

TaC Precipitation Kinetics During Cooling of Co–Re-Based Alloys

Lukas Karge, Ralph Gilles, Michael Hofmann, Debashis Mukherji, Joachim Rösler, Dirk Honecker, Přemysl Beran, Pavel Strunz, Norbert Schell, and Sebastian Busch*

Cobalt–rhenium (Co–Re) alloys are developed for high-temperature applications at $\approx 1200^\circ\text{C}$ and are strengthened by dispersion of nanosized tantalum carbide (TaC) precipitates. Herein, the precipitation behavior during cooling from supersolution depending on the cooling rate and the addition of chromium is presented. The phase composition (matrix phases and TaC) is analyzed from the wide-angle neutron diffraction patterns measured in situ during temperature cycling. The precipitation of nanosized TaC particles is measured by in situ and ex situ neutron and X-ray small-angle scattering. The in situ measurements are used to extract the temperature-dependent volume fraction of the precipitates; the final size distribution after cooling is extracted from the ex situ measurements. A Kampmann–Wagner's numerical (KWN) model is adapted to isochronal cooling processes. The in situ measurements give the unique possibility to calibrate the model parameters, whereas the ex situ measurements are used to assess the model predictions.

mechanical energy, it is still economically and ecologically beneficial to maximize the efficiency of the traditional gas turbine that is widely used, for example, in power plants or jet engines. As it is usually not feasible to lower T_{\min} , this efficiency gain has to be realized by raising T_{\max} . To do so, it is necessary to use materials that can sustain high temperatures and harsh chemical conditions.^[1] For this purpose, conventionally, nickel^[2] and more recently also cobalt-based^[3] alloys are often used. It was found that the material properties of cobalt-based (Co) alloys can be further improved by adding rhenium (Re), which is completely miscible with cobalt and has an extremely high melting point of 3455 K .^[4] In the present contribution, Co–Re alloys with 17 at% of rhenium are used with a melting temperature of $\approx 1970\text{ K}$.^[5]


Precipitated metal carbides, e.g., the monocarbide tantalum carbide TaC, strengthen the Co–Re alloy.^[5–7] Tantalum carbides are attractive because of their stability at elevated temperatures. Furthermore, transmission electron microscopy (TEM) investigations after creep deformation showed pinning of dislocations at the TaC particles due to an attractive particle dislocation

1. Introduction

The upper efficiency limit η of a constant-pressure heat engine is given by the one of the ideal Brayton cycle, $\eta \leq 1 - T_{\min}/T_{\max}$. While the methods of power generation are currently shifting toward methods that do not rely on converting heat to

Dr. L. Karge,^[+] Dr. R. Gilles, Dr. M. Hofmann
Heinz Maier-Leibnitz Zentrum
Technische Universität München
Lichtenbergstr. 1, Garching bei München 85747, Germany

Dr. D. Mukherji, Prof. J. Rösler
Technische Universität Braunschweig
Institut für Werkstoffe
Langer Kamp 8, Braunschweig 38106, Germany

 The ORCID identification number(s) for the author(s) of this article can be found under <https://doi.org/10.1002/adem.202100129>.

^[+]Present address: Daimler AG, Stuttgart, Germany

^[++]Present address: ISIS Neutron and Muon Facility, Rutherford Appleton Laboratory, Science & Technology Facilities Council, Didcot OX11 0QX, UK

^[+++]Present address: European Spallation Source ERIC, Box 176, Lund SE-221 00, Sweden

© 2021 The Authors. Advanced Engineering Materials published by Wiley-VCH GmbH. This is an open access article under the terms of the Creative Commons Attribution License, which permits use, distribution and reproduction in any medium, provided the original work is properly cited.

DOI: 10.1002/adem.202100129

Dr. D. Honecker^[+++]
Large Scale Structures Group
Institut Laue-Langevin
71 avenue des Martyrs, CS 20156, Grenoble cedex 9 38042, France

Dr. P. Beran,^[++++] Dr. P. Strunz
Department of Neutron Physics
Nuclear Physics Institute of the CAS
Řež 130, Řež 25068, Czech Republic

Dr. N. Schell
Institute of Materials Physics
Helmholtz-Zentrum Hereon
Max-Planck-Str. 1, Geesthacht 21502, Germany

Dr. S. Busch
German Engineering Materials Science Centre (GEMS) at Heinz Maier-Leibnitz Zentrum (MLZ)
Helmholtz-Zentrum Hereon
Lichtenbergstr. 1, Garching bei München 85747, Germany
E-mail: sebastian.busch@hereon.de

interaction.^[8] The attraction stems from partial relaxation of the dislocation stress field at the particle–matrix interface.

The strengthening effect is determined by the number of hardening precipitates and their size: too small precipitates are cut by travelling dislocations, too large precipitates are far apart at a given volume fraction and can be circumvented by the dislocations. The optimal size is therefore given by a trade-off between these two limits and was determined to be on the order of 10–100 nm in the present case.^[7] The microstructures observed in the Co–Re–Ta–C system show large Chinese script-like TaC particles at the grain boundaries and a very fine (smaller than 50 nm) dispersion of TaC carbide within the grains and therefore, an ideal microstructure for high temperature creep resistance.^[9,10] The volume fraction of nanosized precipitates is around 1 vol%. To obtain the desired material properties, it is of utmost importance to control the size of these precipitates by appropriate heat treatments.

Further additives can tune other material properties. Boron was studied^[11–13] as it can be used to prevent grain boundary failure and improve ductility^[14] and tune grain size^[5,15] (not used in this study), whereas chromium (Cr) protects the material from the extremely oxidizing environment in a turbine.^[16,17] Also, the addition of other elements like nickel has been the subject of previous studies.^[18,19]

The aim of this study is to investigate the number and size of TaC precipitates in two Co_{80.72–x}Re₁₇Cr_xTa_{1.20}C_{1.08} alloys (numbers denote atomic composition): one without and one with replacing 15 at% of Co by Cr, see **Table 1**. These two alloys, named Co–17Re–0Cr and Co–17Re–15Cr, hereon, are subjected to various heat treatments and the precipitates are studied in situ using neutron and synchrotron X-ray scattering methods. Both methods provide a high penetration depth for high-temperature alloys and are differently sensitive to the studied materials. In addition, neutron methods are well suited due to the large beam cross section for real bulk information,^[20] whereas synchrotron X-ray methods are at an advantage because of higher flux and better temporal and spatial resolution.^[21] While the scattering curves do not give a real-space image of the precipitates, these techniques are ideally suited for measuring the particle properties during heat treatment. Only this in situ monitoring over a reasonable bulk volume gives access to the real precipitation kinetics, which is needed to optimize the production process.

Table 1. Investigated Co–Re alloy types. Co–17Re–15Cr differs only by the addition of 15 at% of Cr while reducing the Co content accordingly from Co–17Re–0Cr. The neutron scattering length values were determined in other studies.^[7,54] It was assumed that TaC precipitates do not contain matrix atoms, their stoichiometry was determined from the lattice constant.^[27] The neutron scattering length density (SLD) for the two alloys is given for the ϵ phase.^[7,15]

Name	Co	Re	Cr	Ta	C	SLD
Unit	at%	at%	at%	at%	at%	10 ¹⁰ cm ⁻²
Co–17Re–0Cr	80.72	17	0	1.20	1.08	3.47
Co–17Re–15Cr	65.72	17	15	1.20	1.08	3.56
TaC phase	—	—	—	58.5	41.5	6.16

These data will be compared with a theoretical model based on the well-known Kampmann–Wagner’s numerical (KWN) approach, adapted for isochronal cooling processes (i.e., with a constant temperature ramp). Predicting the precipitation kinetics was not easy, because the samples were not heat treated at a constant temperature, and precipitation occurred during cooling, moreover in a temperature range where Co–Re-based alloys undergo a phase transformation from a high-temperature face-centered-cubic (fcc, γ) phase to a low-temperature hexagonal-close-packed (hcp, ϵ) phase,^[22] which can be diffusion controlled or martensitic. In pure Co, this transition occurs at around ≈ 690 K,^[23] but it is heavily influenced by additives; for the present alloys, the transition temperature is at around ≈ 1600 K.^[5] In both alloys, there is a temperature range in which γ and ϵ phase can coexist. While the two phases still exist at room temperature for Co–17Re–0Cr, the addition of the hcp stabilizer chromium leads to a complete conversion to the ϵ phase in Co–17Re–15Cr already at elevated temperatures upon cooling.^[5] The types of measurements presented in this study give a unique opportunity to calibrate theoretical models and assess their predictions.

2. Results

Three types of scattering experiments were conducted: small-angle neutron and high-energy synchrotron X-ray scattering (SANS and SAXS) as well as wide-angle neutron diffraction (ND) measurements. Both, neutrons and high-energy X-rays, have a high penetration depth into materials and can therefore probe the bulk properties of the studied alloys. They are some of the few techniques that can study the material properties in situ during heat treatment and average over a large enough sample volume to be statistically significant.^[24,25] As a drawback, the results are encoded in scattering patterns, which are harder to interpret than real-space images.

Wide-angle diffraction is sensitive to the atomic distances in materials and picks up on the amount of crystallized material as well as its crystal structure. Individual phases are identified by sets of Bragg peaks (maxima in diffracted intensity), which reflect the atomic structure of each individual phase. From the shapes of these peaks, it is possible to retrieve microstructure (particle size, microstrain, texture, etc.) information of each phase; this information is not discussed in the present contribution. The intensity of these peaks is proportional to the respective phase fraction in the case of a multiphase material. We used a full-pattern fitting of ND datasets to extract phase transformation start and end temperatures and phase fraction, especially of TaC at each measured temperature, see Supporting Information. By identifying the feature originating from TaC, the amount of crystallized TaC precipitates was extracted from these measurements and, in reverse conclusion, the concentration of Ta that is dissolved in the matrix at any temperature.

Small-angle scattering (SAS) contains information about the nanoscale structure and chemical inhomogeneities (under ideal circumstances ≈ 1 –1000 nm) of the material. To contribute to the SAS signal, the material has to contain inhomogeneities of the scattering length density (SLD) on this length scale. The SLD is the product of the atomic density with the scattering length (i.e., interaction strength) of the atoms. In the case of neutrons, the

scattering length is a tabulated nuclear property; in the case of X-rays, it is in first approximation proportional to the number of electrons and therefore the SLD given by the electron density. The SLD can be easily calculated for any material with known gravimetric density and composition.^[26] The squared difference of the SLD of the inhomogeneities with respect to the matrix determines the particle scattering contrast, which is in general different for SANS and SAXS. The size of inhomogeneity is encoded in the Q -dependence of the scattered intensity, where Q is the magnitude of the scattering vector, calculated as $Q = 4\pi \cdot \sin(2\theta/2)/\lambda$ from the scattering angle 2θ and the neutron/X-ray wavelength λ . The scattered intensity is proportional to the product of the volume fraction and the scattering contrast. In addition to the features in the scattering curve, there is always a background in the data, which is not experimental noise but inherent to the samples due to incoherent fluctuations or disorder.

It is important to note that SAS is sensitive to nanosized variations in the SLD rather than the crystal structure, which determines the ND signal. Although these two effects often go hand in hand, that is not necessarily the case: be it varying atom concentrations within a single crystal (yielding SAS but no additional peak in wide-angle diffraction), different crystal structures where atomic density and scattering length happen to balance each other out (visible by diffraction but not SAS), or simultaneous creation of nanosized and micrometer-sized precipitates (both result in a wide-angle diffraction peak but only the nanocrystals are visible in SAS).

2.1. Wide-Angle ND

The different crystalline phases in the alloy generate Bragg peaks in the ND diffractogram that can be assigned based on their scattering vector, see **Figure 1** and Supporting Information. The samples were cooled slowly in steps of 20 K to probe near-equilibrium quantities. For experimental details, see Section 5. The intensity color plots shown in Figure 1 display the relevant parts of ND patterns in Q -space as a function of temperature for both samples. The peaks are labeled by the phase name and Miller indices hkl . In addition to the matrix phases

Table 2. Temperatures of different events in the two studied alloys during slow cooling. The transformation of the matrix crystal structure $\gamma \rightarrow \epsilon$ and the precipitation of TaC particles, seen either by wide-angle ND or by SANS. Where extracted, the start and end temperatures of the transitions are given.

Transition	Method	Point	Co–17Re–0Cr [K]	Co–17Re–15Cr [K]
$\gamma \rightarrow \epsilon$	ND	Start	1553	1603
$\gamma \rightarrow \epsilon$	ND	End	–	1523
TaC form	ND	Start	1746	1611
TaC form	SANS	Start	1390	1580
TaC form	SANS	End	–	1520

and TaC, there is also a peak caused by Al_2O_3 , which was used as the sample holder. This signal decreases in intensity as the temperature is lowered as the sample stick shrinks and the holder moves out of the beam.

At the highest temperature (1773 K) for both samples, the matrix consists only of γ phase. Upon cooling, the matrix starts to transform from γ to the ϵ phase at 1553 K (Co–17Re–0Cr) and 1603 K (Co–17Re–15Cr), respectively. This transformation ends in the chromium-containing sample at 1523 K, where the complete matrix is in the ϵ phase. In the case of the sample without chromium, the γ phase remains visible down to room temperature^[5] (see also **Table 2**).

Also the formation of TaC proceeds differently in the two samples: In Co–17Re–0Cr, the TaC Bragg peak is already visible at very high temperatures in Figure 1 and increases gradually in intensity. In the case of Co–17Re–15Cr, scattered intensity is visible only at much lower temperatures and increases then rapidly. This signal is evaluated in detail in the following sections.

The dissolved concentration of Ta in equilibrium $c_{\alpha, \text{eq}}$ in the Co–Re matrix was calculated from these measurements during slow cooling. It has to be noted that several simplifying assumptions were made in the present contribution, which influence the parameters extracted from the model presented in Section 2.3, but neither the overall picture nor the way to validate the model demonstrated here. The approximations will be mentioned in the following sections and discussed in detail later.

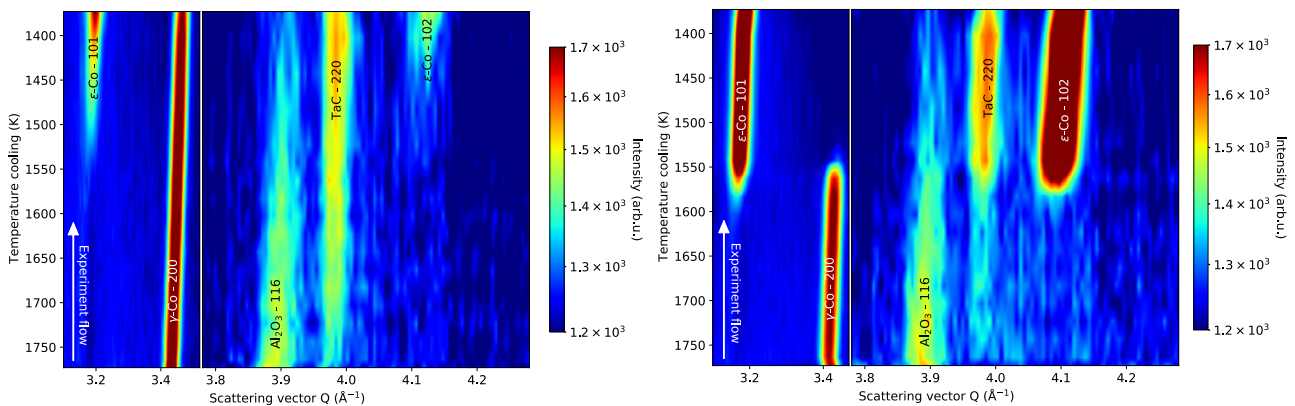


Figure 1. Intensity color maps of relevant parts of wide-angle ND patterns for Co–17Re–0Cr (left) and Co–17Re–15Cr (right) as a function of scattering vector and temperature. The Bragg peaks are labeled by phase name and Miller indices. Al_2O_3 was used as the sample holder. The slight shift of all peaks with varying temperature is attributed to thermal expansion.

The evolution of TaC peaks is shown in Figure 1: the peak intensity assigned to TaC is proportional to the phase fraction of crystalline TaC precipitate. A full Rietveld refinement was conducted at each temperature to extract the intensities discussed in the following section. The temperature-dependent Debye–Waller factor was taken into consideration during the analysis. A simplifying assumption was made, where the equilibrium Ta solubility in the matrix at room temperature (RT) is zero, and therefore all TaC is precipitated during the measurement at the lowest temperature. The corresponding peak intensity then reaches its maximal value given by c_0 , the nominal Ta content in the alloy, and one can extract the fraction of dissolved Ta at any temperature by comparing the measured peak intensity at this temperature T , $I_{\text{TaC}}(T)$, with the maximal value $I_{\text{TaC}}^{\text{max}}$.

$$c_{\alpha,\text{eq}}(T) = c_0 \cdot \left(1 - \frac{I_{\text{TaC}}(T)}{I_{\text{TaC}}^{\text{max}}}\right) \quad (1)$$

The resulting $c_{\alpha,\text{eq}}(T)$ determined by Equation (1) for the two alloys is shown in Figure 2. The approximation of complete TaC precipitation after cooling might indeed not be suitable for Co–17Re–0Cr, as will be discussed later.

The dissolved fraction was further approximated with a simple exponential function of the type

$$c_{\alpha,\text{eq}}(T)/c_0 = \min(1, p \cdot \exp(T - T_{\text{start}})) \quad (2)$$

with an onset temperature of TaC precipitation during cooling determined by ND T_{start} and a prefactor p determining the sensitivity of the precipitated amount on the temperature drop. For the two alloys, the obtained fit parameters were Co–17Re–0Cr which has a T_{start} of 1746 K and a p of 4.1×10^{-3} , whereas Co–17Re–15Cr has T_{start} of 1611 K and a p of 15.1×10^{-3} (see also Table 2). This approximation, in turn, does not reproduce the data points of Co–17Re–15Cr very well.

After cooling to room temperature, the carbon-to-tantalum ratio (nominal: C/Ta = 0.9) in the TaC particles was determined by ND from the lattice constants^[27] as Co–17Re–0Cr: lattice constant 4.4435(1) Å, C/Ta = 0.9 and Co–17Re–15Cr: lattice constant 4.4247(2) Å and C/Ta = 0.75.

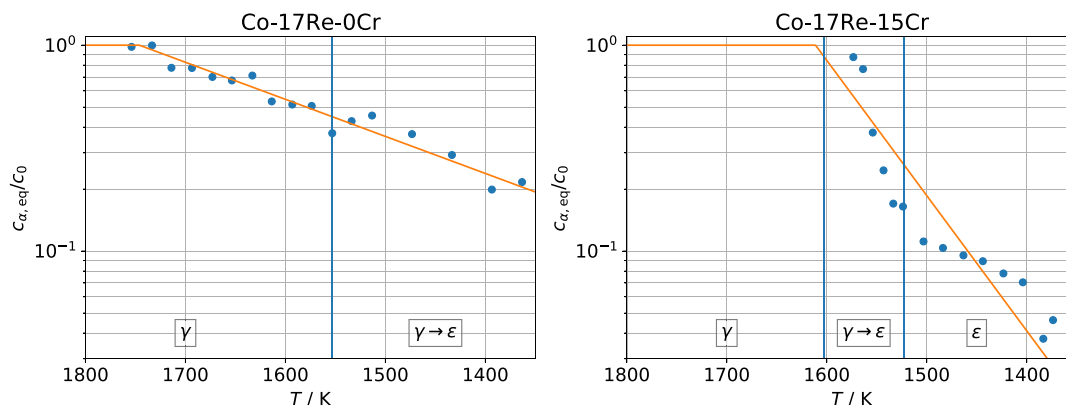


Figure 2. Normalized solubility of Ta in the Co–Re matrix versus temperature, determined by ND during cooling in Co–17Re–0Cr (left) and Co–17Re–15Cr (right), approximated with a simple exponential function, see text. The matrix phases and their transformation temperatures, also determined by ND, are shown in the graphs as vertical blue lines.

2.2. Small-Angle Scattering

Basically all engineering-relevant materials have two contributions to the SAS intensity with rather limited information, especially in the present use case. 1) At low Q , there is a Porod background, proportional to Q^{-4} , that originates from very large-scale SLD fluctuations with a broad size distribution in the sample.^[28] In Co–Re alloys, its main origins are grain boundaries between ϵ and γ matrix phase and large-scale faceted TaC particles ($\approx 1 \mu\text{m}$).^[7] 2) At high Q , there is a constant background. Both contributions can overpower the scattering signal from the precipitates in a wide Q -range and therefore complicate the interpretation.

Nevertheless, at the supersolvus temperature 1773 K, all Ta is in solution and therefore the signal is purely of Porod type.^[29] A fit to this signal by $a \cdot Q^{-4} + b$ is used as background in the data evaluation (b was linearly interpolated between the 1773 K and RT measurement, whereas a was extracted only from the 1773 K measurement; both were determined independently for SAXS and SANS). From previous studies, it is known that the only scattering structures in the monitored Q -range are nanosized TaC precipitates.^[7,29] Their time and temperature-dependent coherent scattering signal is therefore obtained from the measured signal I by subtracting the background

$$S_{\text{coh,TaC}}(Q, T, t) = I(Q, T, t) - a \cdot Q^{-4} - b(T) \quad (3)$$

2.2.1. Ex Situ SAS

Several identical samples were cooled with different rates and compared at room temperature. After raw data treatment, ex situ data covering the full Q -range with high count statistics (see Figure 3) were evaluated by model-based fitting. Given the covered Q -range, precipitates with a diameter of roughly 10–250 nm should be visible. A spherical form factor with a log-normal radius distribution was assumed for the coherent scattering signal of the precipitates $S_{\text{coh,TaC}}$. Interparticle interference effects were considered during the evaluation, but a structure

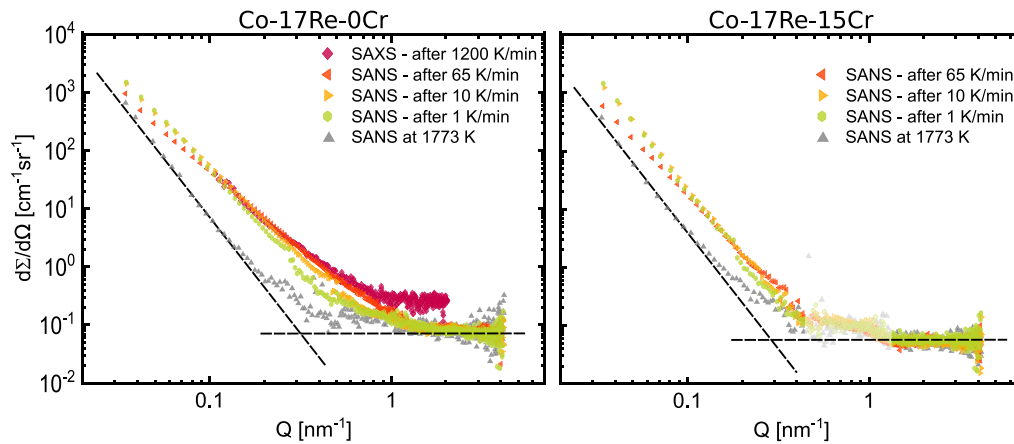


Figure 3. Measured SAS curves at room temperature after cooling the alloys with different rates. Also shown is the background scattering at the supersolus temperature 1773 K (gray points) as well as guides to the eye of a Q^{-4} Porod background as well as the constant background at high Q (dashed lines). The constant background of SAXS is higher than the one of SANS. For Co–17Re–15Cr, detector problems occurred at intermediate Q ; the corresponding points were grayed out and were not taken into consideration for the analysis. Faster cooling rates result in intensity scattered to higher Q , indicating smaller precipitates.

factor (e.g., hard sphere) did not influence the results, as the TaC volume fraction is low (a few percent).

Both probes, synchrotron X-rays and neutrons, show generally the same behavior apart from a higher constant background in SAXS. This is to be expected as there is only one type of precipitate, so both probes are scattered by the same particles. The data of both alloys show a broad increase in scattered intensity at around 0.1 nm^{-1} after cooling from the supersolus temperature. This intensity is caused by TaC precipitates that do not exist at 1773 K. Increasing the cooling rate shifts scattered intensity from low Q to high Q , indicating that the size distribution of the precipitates shifts toward smaller diameters. This is corroborated by the fit results of the model analysis shown in **Figure 4**. The overall scattering intensity, however, is similar in the four curves, suggesting a similar volume of TaC precipitation. Comparing the two alloys, it can be seen that the addition of chromium leads to larger precipitates, in particular, at the slow cooling rates of 10 and 1 K min^{-1} . It should be noted that these precipitates are very large for SAS measurements, the corresponding size distributions should therefore be taken with a grain of salt.

The volume fraction of nanosized TaC precipitates seen by SAS was determined to be 0.92–0.98 vol% for Co–17Re–0Cr (depending on cooling rate) and 1.47–1.51 vol% for Co–17Re–15Cr, see **Table 3**.

2.2.2. In Situ SAS

To get information about nucleation, growth, and coarsening of the nanosized TaC precipitates during cooling from a supersaturated solution, fast SAS measurements were carried out during the temperature change: every 15 s for SANS and every 1 s for SAXS. Due to the significantly lower statistics than that in the ex situ measurements, the fast measurements were not evaluated by fitting a model but instead by extracting two integral parameters: the radius of gyration from a Guinier plot and the volume fraction from the Kratky function.

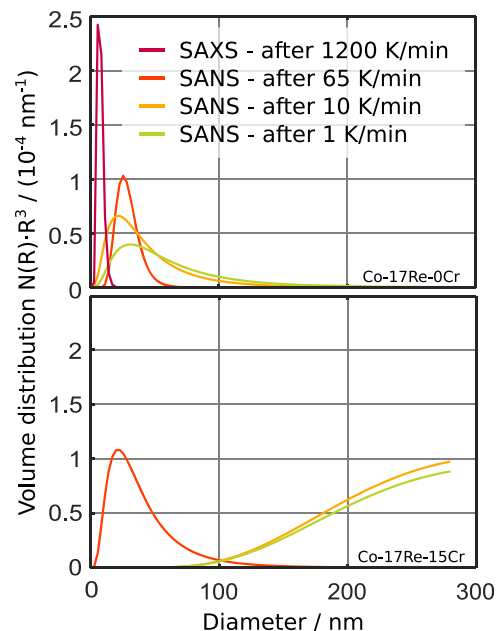


Figure 4. Volume-weighted size distributions of the precipitates extracted from model fits to the ex situ SAS data of Co–17Re–0Cr (top) and Co–17Re–15Cr (bottom). The trend of faster cooling rates resulting in smaller precipitates is clearly visible. The addition of chromium results in the formation of larger precipitates.

Table 3. Precipitated volume fraction of nanosized TaC for different cooling rates after cooling from 1773 K to RT.

TaC vol.fr. [%]	1 [K min ⁻¹]	10 [K min ⁻¹]	65 [K min ⁻¹]	1200 [K min ⁻¹]
Co–17Re–0Cr	0.98	0.97	0.93	0.92
Co–17Re–15Cr	1.50	1.51	1.47	

For very small Q ($Q \cdot R_G \ll 1$), the precipitate SAS scattering contribution can be described by Guinier's approximation^[28]

$$S_{\text{coh,TaC}}(Q) = \exp[-(QR_G)^2/3] \quad (4)$$

The radius of gyration R_G is the root mean square of the distances within a scattering particle from its center of gravity and can be understood as the particle size. It can be extracted from the initial slope m of the function $\log S_{\text{coh,TaC}}(Q^2)$: $R_G = \sqrt{-3m}$. This number gives an average over the whole sample and does not allow to evaluate the particle size distribution further.

The volume fraction of scattering particles f_p can be linked to the scattering invariant Q_{inv} , the integral of the Kratky function $Q^2 \cdot S(Q)$.^[30]

$$Q_{\text{inv}} = \int dQ Q^2 \cdot S_{\text{coh,TaC}}(Q) = 2\pi^2 V \Delta\rho^2 f_p (1 - f_p) \quad (5)$$

where V is the sample volume and $\Delta\rho$ the SLD difference between precipitate and matrix. In the case of a dilute two-phase system, f_p is small and $f_p(1 - f_p) = f_p - f_p^2 \approx f_p$; hence, $f_p \propto Q_{\text{inv}}$. Both assumptions are valid for the present types of Co–Re alloys, as there are no other phases in the SANS resolution range and $f_p \approx 1$ vol% of TaC precipitates.

Figure 5 shows a comparison of the in situ-measured SANS curves of Co–17Re–0Cr during cooling with 65 K min^{-1} and the SAXS curves during rapid quenching with 1200 K min^{-1} . The depicted curves are a manual selection of temperatures and show the increase in scattering as a result of the emerging nanosized TaC precipitates. The limited Q -range of the in situ measurements means that only particle diameters in the range of roughly 10–50 nm (SANS) or 10–25 nm (SAXS) can be detected. The curves are rather noisy due to the high time resolution of the experiment. As described earlier, the scattering signal at 1773 K is regarded as background; the evaluated scattering signal caused by the precipitates is only the part on top of this.

The radius of gyration and volume fraction were extracted from the Guinier and Kratky functions, respectively, for every dataset of the in situ cooling measurements. The results are

shown together with contour plots of the Kratky functions in **Figure 6** and 7. The matrix phase transitions as determined by wide-angle ND are also shown.

For Co–17Re–0Cr, nanosized TaC precipitates are only starting to be visible at temperatures below the beginning of the $\gamma \rightarrow \epsilon$ matrix phase transformation. The onset temperature of $\approx 1390 \text{ K}$ does not depend very much on the cooling rate (except for the 1200 K min^{-1} quench). The observed TaC particle gyration radii are in the order of 20–40 nm. As more particles precipitate at lower temperature, the average radius of gyration decreases for the measurements with moderate cooling rates; the size during the 1200 K quench increases initially as the temperature decreases and stays constant during the bulk of the precipitation process. Increasing the cooling rate leads to an increase of the volume fraction at lower temperatures and precipitates with smaller radii.

For Co–17Re–15Cr, it can be seen that the transformation starts at higher temperatures ($\approx 1580 \text{ K}$) as a result of chromium addition, but also only below the start of the $\gamma \rightarrow \epsilon$ matrix phase transition. The majority of precipitation is complete at $\approx 1520 \text{ K}$, see Table 2. The particle radii of gyration are in the order of 30–38 nm. Just like for Co–17Re–0Cr, increasing the cooling rate leads to an increased volume fraction of precipitates at lower temperatures and to smaller particles.

2.3. Modeling Nucleation and Growth Kinetics

Precipitation can be modeled by a nucleation step, followed by particle growth, and finally coarsening. As all experiments discussed here were rather short (under 2 h), it will be assumed that the observed particles only exhibit growth but coarsening is not visible yet. A common model for the nucleation and growth process at constant temperature is the KWN model.^[31,32] It was recently extended to isochronal cooling processes.^[33,34] In the frame of this work, the in situ measurements of precipitate solubility in the matrix and volume fraction of nanosized precipitates were used as constraints to the model. The details can be found in the Supporting Information,^[5] a summary follows here.

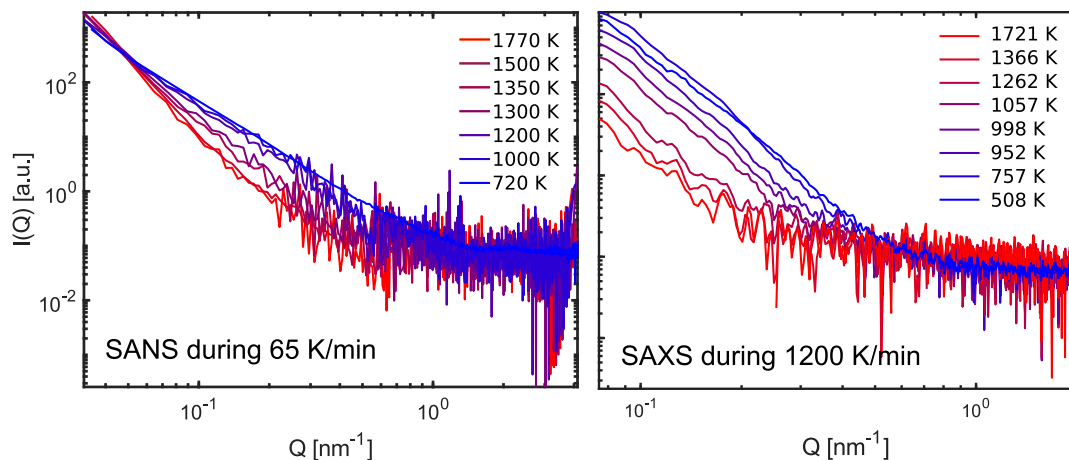


Figure 5. Comparison of the in situ SANS (left) and SAXS (right) curves during cooling with ramps of 65 and 1200 K min^{-1} , respectively. The precipitation of nanosized TaC can be followed by the increasing SAS intensity.

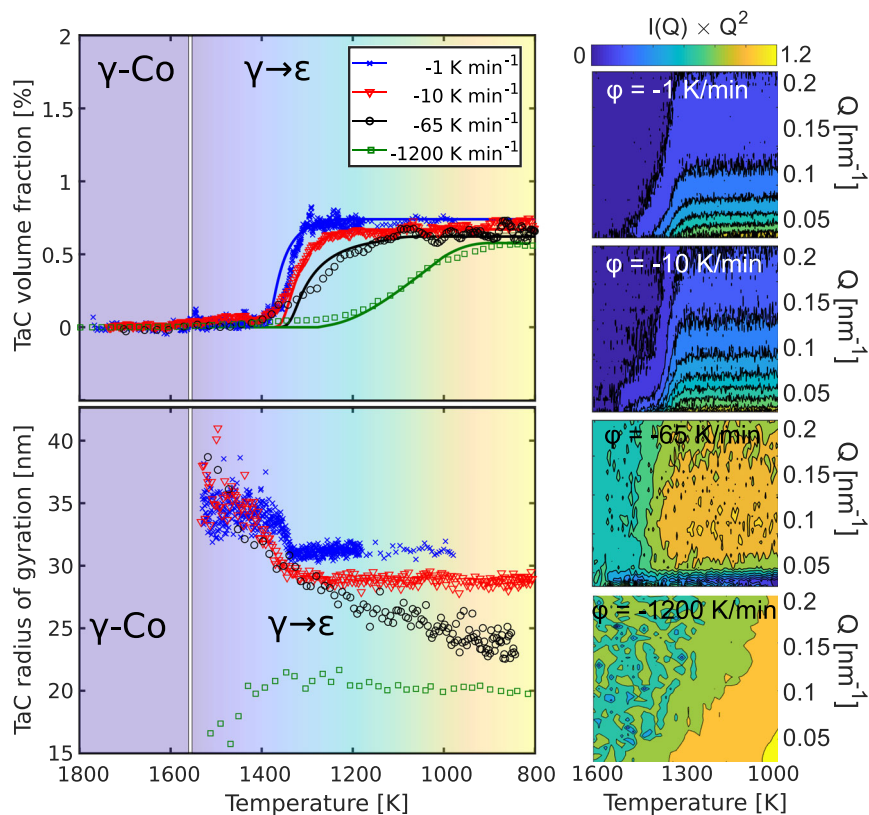


Figure 6. TaC precipitate volume fraction (top left) and average radius of gyration (bottom left) during cooling of Co–17Re–0Cr with rates of 1, 10, 65, and 1200 K min⁻¹. Drawn-out lines are the results from the KWN evaluation, see Section 2.3. Right: Kratky surfaces during cooling with different cooling rates. The plots show the distribution of SAS from nanosized particles in reciprocal space. The maximum Q -value of scattering intensity corresponds to the minimum precipitate size. Therefore, lower cooling ramps result in larger particles.

The prototypical implementation of the model discussed here did not propagate the experimental error bars. Even though the underlying material system exhibits a fairly complex behavior itself, the model can replicate the observed quantities. The aim is to obtain values for speed and temperature dependence of nucleation and growth characterized by a frequency factor D and activation energy Q (assuming an Arrhenius behavior^[35]) and the particle–matrix interface tension Γ using the experimentally determined solubility of Ta in the matrix (ND) and optimizing the parameter values to reproduce the precipitated volume fraction of nanosized TaC (measured by in situ SAS) at each temperature and for all cooling rates. The model then predicts the final precipitate size distributions for the different cooling rates, which can be plotted with the results of ex situ SAS measurements.

Nucleation was considered to be homogeneous. As foreseen in the KWN model, there is a time lag between reaching oversaturation of the elements associated with the dissolved phase in the matrix and the start of precipitation. The total Gibbs energy is given by the demixing of the supersaturated mixture on one side and the interfacial energy plus the deformation energy on the other side. The interfacial energy is given by the interface tension Γ , the deformation energy can be estimated using the shear modulus of the matrix and the effective bulk modulus of the particle. This requires

the molar volumes v of the precipitate and matrix as well as the elastic strain energy induced by the precipitates g_{el} (see Supporting Information). The particles have to reach a critical radius at which the energy gain (proportional to the particle volume) outweighs the penalty (proportional to its interface to the matrix). After crossing this nucleation energy barrier, the growth regime follows.

During growth, particles above the critical radius grow further, driven by the supersaturated dissolved elements in the matrix. The growth speed depends on the concentration of tantalum and carbon in the matrix and their diffusion coefficients. Both change constantly during the isochronal cooling process because the ongoing precipitation reduces the concentration of the dissolved elements and the changing temperature reduces the diffusion coefficient. As carbon is a much smaller atom than the others and can move relatively freely on interstitial sites, its diffusion coefficient is so high that only the Ta diffusion coefficient is the rate-limiting factor.^[35–37]

In a final step, the particles coarsen to reduce the total interface area between particles and the matrix by growing big particles on the expense of small ones. As this happens over a much longer time scale than the measurements presented here, it was neglected in the current model.

The unknown variables (interface tension Γ , frequency factors for nucleation and growth D_N, D_G , and activation energies for

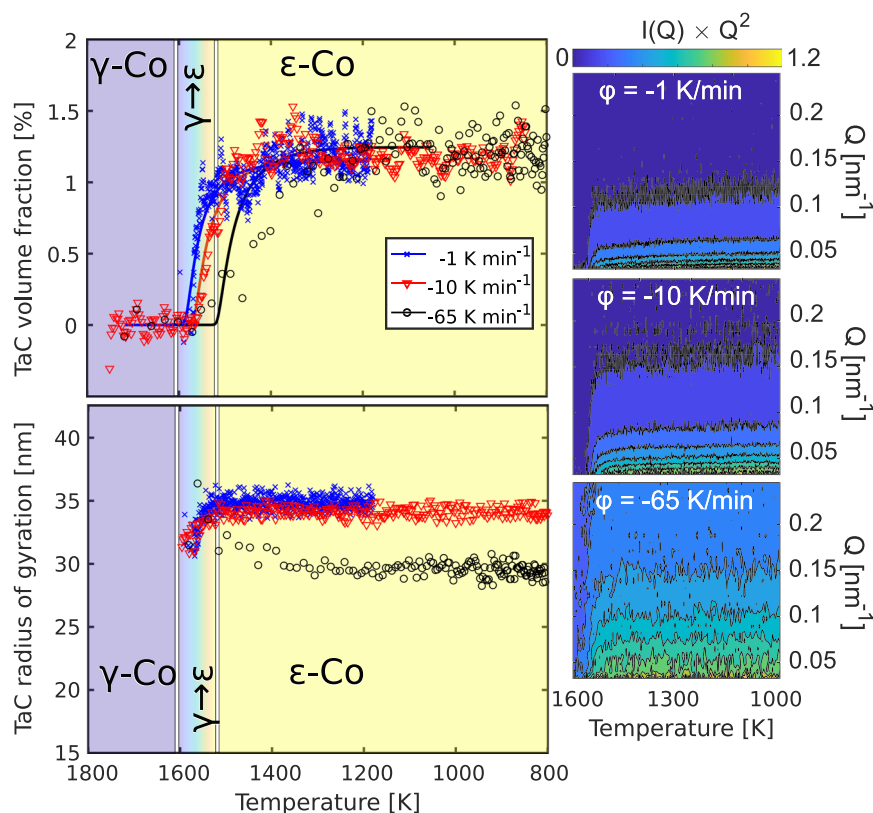


Figure 7. TaC precipitate volume fraction (top left) and average radius of gyration (bottom left) during cooling of Co–17Re–15Cr with rates of 1, 10, and 65 K min⁻¹. Drawn-out lines are the results from the KWN evaluation, see Section 2.3. Right: Kratky surfaces during cooling with different cooling rates. The plots show the distribution of SAS from nanosized particles in reciprocal space. The maximum Q -value of scattering intensity corresponds to the minimum precipitate size.

nucleation and growth Q_N, Q_G) are expected to be independent of the cooling rate. For a more robust parameter determination, the various cooling measurements of the materials were therefore fit simultaneously. Only the data of the 1200 K min⁻¹ quench was excluded as the model was clearly not able to reproduce the data (the dataset was still modeled by the modified KWN approach).

The fit algorithm is explained in detail in Supporting Information. It takes the temperature-dependent Ta solubility from ND measurements as input as well as some tabulated material properties like bulk moduli. Also, initial parameters for the unknown variables have to be supplied. The precipitation is then modeled with one parameter set over the whole temperature range for all measured cooling rates simultaneously. The precipitated volume fraction is extracted as a function of temperature and compared with the one that is extracted from the in situ SAS measurements over the whole temperature range. The fitting algorithm tries to minimize the mean-squared deviation between the computed temperature-resolved volume fraction and the measured volume fraction.

The particle size distributions are extracted at the end of the cooling process and compared with the size distributions determined from the ex situ SAS measurements. The unknown parameter values are then varied until an optimal match between the model prediction and the measurement is obtained.

The temperature-dependent evolution of the precipitated volume fraction of model and in situ measurements is compared in Figure 6 and 7. The final precipitate size distribution after cooling is compared with the experimental results of the ex situ measurements in Figure 8. The in situ determination of the radius of gyration was found to be too approximate to help with confining the model.

A comparison of the model results with the in situ-measured nanosized TaC volume fraction in both alloys is shown in the respective figures (Figure 6 and 7). The reason for more delayed precipitation at higher cooling rates can be replicated by the adapted KWN model for isochronal cooling and has a twofold explanation: 1) the nucleation rate equation includes a term for the incubation time of nucleation. This term delays the start of the phase transformation for high cooling rates. 2) Precipitation is limited by the diffusional growth of the particles. The growth is a function of time and therefore the higher cooling rates result in smaller growth.

Table 4 shows the fit results for both alloys from the adapted KWN model. The parameters for each alloy were fitted simultaneously to the data from the respective cooling ramps. The difference in precipitation behavior therefore only depends on the cooling ramp, which is a parameter for particle growth and nucleation rate. A larger cooling ramp results in less time for particle growth and therefore the matrix is strongly supersaturated at lower temperatures.

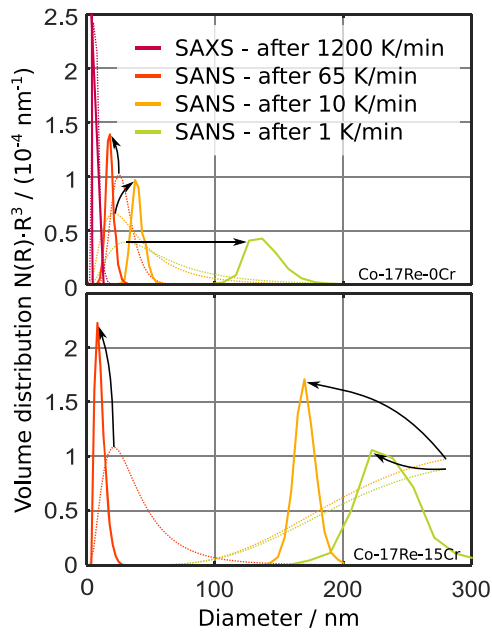


Figure 8. Volume-weighted size distributions of the precipitates extracted from the modified KWN model (bold lines), compared with the results of fits with the ex situ SAS data (thin dots) shown also in Figure 4. Top Co-17Re-0Cr and bottom Co-17Re-15Cr.

3. Discussion

3.1. Wide-Angle ND

Wide-angle diffraction is sensitive to all forms of crystalline TaC: not only the strengthening nanosized TaC precipitates, but also large faceted TaC in the matrix and blocky TaC at grain boundaries.^[6] By picking up on the total amount of crystalline TaC, diffraction is suitable to determine the concentration of still dissolved Ta in the matrix, but not the volume fraction of nanosized precipitates, which is rather to be measured by SANS.

The simple fit of Ta solubility extracted from wide-angle ND in Figure 2 with an exponential function works well in the case of Co-17Re-0Cr. In this alloy, the $\gamma \rightarrow \epsilon$ phase transformation (also determined by ND) starts at ≈ 1553 K and proceeds slowly, not finishing even at room temperature. TaC precipitation is detected by ND already from ≈ 1746 K, well above the matrix phase transition temperature, when the sample is still completely in the γ phase. The C/Ta ratio of 0.9 determined for these samples at room temperature is closer to the stoichiometric

composition than the ratio in Co-17Re-15Cr (where it is 0.75, see below), which might explain the enhanced high-temperature stability of TaC precipitates in Co-17Re-0Cr.

In contrast, the single exponential does not capture the obvious two regimes of the Ta solubility in Co-17Re-15Cr. This alloy has a higher onset temperature of the matrix phase transformation of ≈ 1603 K and is completely transformed into the ϵ phase at 1523 K. The relatively sudden $\gamma \rightarrow \epsilon$ phase transformation in Co-17Re-15Cr overlaps strikingly with a sudden drop in Ta solubility. A lower Ta solubility in ϵ compared with the γ phase is consistent with scanning electron micrographs.^[5] TaC forms and grows more readily in the ϵ phase and chromium stabilizes the ϵ phase. While a different fit function should be used in future works, it should be noted that the Ta solubility is always captured within a factor of ≈ 2 by this simple function, which therefore serves well for the current purpose. The influence of Cr on the C/Ta ratio in TaC precipitates (0.75 instead of 0.9) might be exerted via the high formation temperature of basically all TaC precipitates.

3.2. Small-Angle Scattering

SAS is only sensitive to nanosized inhomogeneities. From scanning electron microscopy micrographs, it is known that the only objects that appear on this length scale are TaC precipitates.^[5]

3.2.1. Ex Situ SAS

At the supersolvus temperature, 1773 K, the SAS signal consists only of a Porod-type background (Figure 3). The corresponding absence of any nanosized inhomogeneities in the sample is consistent with the absence of crystalline TaC determined by ND.

The ex situ SANS experiments show that the final TaC precipitate size depends strongly on the applied cooling rate with faster cooling resulting in finer precipitates; see Figure 4. This is to be expected as the sample spends less time at sufficiently high temperatures to allow for the diffusion that leads to precipitate growth. The overall scattering intensity does not change dramatically between the different cooling rates, suggesting a similar volume of TaC precipitation. This is confirmed by the results of the model fits, which show a slight decrease in precipitated volume fraction at higher cooling rates (Table 3).

Comparing the two alloys, it becomes clear that the addition of chromium leads to a significantly higher volume fraction of precipitated nanosized particles, which are also bigger than those without chromium. As Ta solubility decreases at higher

Table 4. Fixed parameters derived from literature values and fit parameters obtained in this contribution, see Supporting Information for details. All cooling rates (except 1200 K min^{-1}) were fit simultaneously with the same parameter set. The fixed parameters are the molar volumes ν of matrix and precipitate as well as the elastic strain energy induced by the precipitates g_{el} . From the optimized model, the extracted parameters were the interfacial tension Γ and frequency factors D with activation energies Q for nucleation (N) and growth (G).

	Fixed parameters			Fitted parameters				
	$\nu_{\text{Co-Re}}$	ν_{TaC}	g_{el}	Γ	D_N	Q_N	D_G	Q_G
	$10^{-6} \text{ g cm}^{-2}$	$10^{-6} \text{ g cm}^{-2}$	10^9 J m^{-3}	J m^{-2}	$10^{-5} \text{ m}^2 \text{ s}^{-1}$	kJ mol^{-1}	$10^{-5} \text{ m}^2 \text{ s}^{-1}$	kJ mol^{-1}
Co-17Re-0Cr	6.96	6.65	736	0.55	5.0	270	1.5	365
Co-17Re-15Cr	6.96	6.65	736	0.57	5.2	307	2.1	296

temperatures in Co–17Re–15Cr, the precipitate formation takes place at higher sample temperatures where the diffusion coefficients are larger. This allows for more diffusion-limited nucleation and growth of the particles.

The lower volume fraction of nanosized precipitates in Co–17Re–0Cr compared with Co–17Re–15Cr can be explained in different ways. First, in both cases, all TaC might have precipitated but in very different morphologies (nanosized vs. large faceted or blocky TaC). Second, there could still be tantalum and carbon dissolved in the matrix, kinetically hindered from precipitating. Heating experiments indeed show a sudden burst of additional TaC precipitation once high-enough temperatures are reached to mobilize the atoms.^[5] In this case, Equation (1) would have to be modified to have constant nonzero limit for the equilibrium Ta solubility at low temperatures. Third, one could imagine that while all TaC has precipitated in the ϵ phase, the Co–17Re–0Cr alloy still has regions of metastable γ phase, in which tantalum and carbon are still dissolved. The burst of TaC precipitation upon heating could then be attributed to the transformation of the rest of the metastable γ phase to the ϵ phase. In this case, particle nucleation and growth occurs only in the ϵ phase, where the assumption of zero solubility at room temperature is valid, but it would be questionable whether the ND measurements, averaging over ϵ and γ phase, yield useful information about the concentration of dissolved Ta in the ϵ phase.

3.2.2. In Situ SAS

The in situ SAS experiments had to be conducted with a reduced Q -range (see Figure 5) because a change of the instrument geometry (variation of collimation and sample detector distance to obtain a different Q -range) takes a few minutes. This limitation reduces the accuracy of the particle size determination, in particular for SAXS, which might underestimate the sizes. Also, the limited statistics allowed only for the extraction of an averaged radius of gyration as a measure for the particle size, which is of course much less expressive than the complete particle size distribution that can be extracted from the ex situ measurements. This is also the reason why the model was fit to the in situ volume fraction and the ex situ size distributions.

In Co–17Re–0Cr, the SAS measurements pick up on TaC precipitates only at temperatures significantly below the start of the $\gamma \rightarrow \epsilon$ matrix phase transformation, even at very slow cooling rates of 1 K min^{-1} (Figure 6). Once the measurements are sensitive to the precipitates, they already have a size of around 30 nm, meaning that we do not see the nucleation stage but particles are already well into the growth regime. With ND, crystalline TaC is already detected at temperatures above the $\gamma \rightarrow \epsilon$ matrix phase transformation. A possible mechanism for suppressing the growth of these nuclei over a wide temperature range might be the sluggish phase transformation of the matrix. We speculate that larger volumes of the ϵ matrix phase are necessary in which the TaC precipitates can grow.

The precipitated volume fraction shows that for cooling rates of 1 and 10 K min^{-1} , the whole precipitation process occurs at temperatures above $\approx 1250 \text{ K}$, where the particles are rather large—the hotter, the larger due to the enhanced Ta diffusion. In contrast, the volume fraction during the quench with

1200 K min^{-1} shows that this is roughly the temperature where precipitation starts. The slower diffusion at these temperatures leads to the creation of smaller precipitates. The cooling rate of 65 K min^{-1} spans both regimes: while particles formed at high temperatures have similar sizes with the ones of the slower cooling rates, precipitation continues to substantially lower temperatures, where an increasing number of new smaller particles gradually decreases the average radius of gyration.

In Co–17Re–15Cr, precipitates create a SAS signal basically immediately after the beginning of the $\gamma \rightarrow \epsilon$ matrix phase transformation at the slowest cooling rate, with a small kinetic delay for the higher cooling rates (Figure 7). Also in these measurements, the detected particles have already sizes of around 30 nm, meaning that the measurement setup was not sensitive to the initial nucleation phase of the particles.

The whole precipitation process starts and ends at higher temperatures than in the Co–17Re–0Cr sample. As no more (small) precipitates are formed at low temperatures, the average radius of gyration does not decrease gradually toward lower temperatures.

3.3. Modeling Nucleation and Growth Kinetics

The KWN model, which has been widely adopted as a precipitation modeling framework at constant temperature accounting for concurrent nucleation, growth, and coarsening kinetics, was adapted to isochronal cooling (see Supporting Information and refs. [5,34]). Particle coarsening was neglected in this contribution.

The parameters were fit to optimize the agreement with the experimentally in situ-determined precipitated volume fractions for all cooling rates simultaneously. It was not only possible to reproduce the precipitated volume fractions satisfactorily (Figure 6 and 7) but also the ex situ size distributions predicted by the model are in qualitative agreement with the experimental ex situ results (Figure 8). It should be noted that the $\gamma \rightarrow \epsilon$ phase transition of the matrix and Ta solubility were probed in thermodynamical equilibrium by ND, which is not necessarily the case during the faster cooling ramps. The phase transitions shown in Figure 6 and 7 can therefore be shifted to lower temperatures in the in situ experiments, especially for the higher cooling rates.

The model considers nucleation to be homogeneous. As the matrix phase transformation occurs in the same temperature interval as the precipitation, TaC nucleation and growth will be influenced by the introduction of lattice defects and boundaries. These defects can act as nucleation sites in the matrix and the assumption of homogeneous nucleation might be questionable. In this case, the nucleation is heterogeneous, which results in smaller nucleation barriers. As the matrix transformation is quick and complete in the chromium-containing Co–17Re–15Cr but sluggish and incomplete in Co–17Re–0Cr,^[29] the assumption of homogeneous nucleation is more likely justified for Co–17Re–15Cr than for Co–17Re–0Cr. The activation energies for growth, however, are in a similar range as the determined activation energies for diffusion,^[5,35] supporting the assumption of diffusion limited growth.

The model reproduces the general behavior: for the smaller cooling ramps, the distributions have a larger width and particles

grow to larger sizes (Figure 8). This is an expected result, as the slower cooling rates leave more time for particle growth. The mean sizes are in the same order as the distributions measured by ex situ SAS, but the shapes of the distributions are considerably different. It has to be considered that perfect agreement cannot be expected as the experimental ex situ size distributions were evaluated by a model-based fit, whereas the adapted KWN model was fit to reproduce the results of the Kratky surface. Also, coarsening effects were not included in modeling. As shown previously,^[7] the coarsening of nanosized TaC precipitates occurs on a time scale of 10–60 min, depending on the exact temperature, and therefore plays a role during the cooling experiments. The slow cooling ramps of 1 and 10 K min⁻¹ could therefore be influenced by coarsening, especially for the Co–17Re–15Cr sample, where more precipitates are formed at higher temperatures.

The model is able to reproduce the time lag of the creation of precipitates. Therefore, the fast cooling ramps show undercooling before considerable volume fractions are precipitated. Moreover, the growth is diffusion limited and therefore also depends on time. Therefore, the growth starts at lower temperatures for faster cooling ramps, when the chemical driving force is larger due to the temperature-dependent supersaturation of the matrix.

A coherence relationship of the fine TaC precipitates to the ϵ matrix was found.^[7] Small precipitates are likely to nucleate coherently to reduce their interface energy. During the growth of the precipitate, the introduction of dislocations into the interface is readily observed to reduce the misfit energy. The applied model for the induced elastic strain energy from the particle in the matrix expects fully coherent, spherical precipitates and neglects dislocation effects. In reality, the embedding might be anisotropic, i.e., the particles are semicoherent to the matrix.

The fits are sensitive to the experimentally determined Ta solubility in the matrix. There are several factors limiting the accuracy of this value. First, the TaC phase constitutes only a volume fraction of $\approx 1\%$ of the sample and the corresponding Bragg peaks are therefore comparatively small, making them harder to extract. Second, the assumption that the concentration of Ta in the matrix drops to zero at room temperature is not necessarily fulfilled. Third, the simple exponential decay of the solubility could be replaced by a more appropriate function.

Values for the interfacial tension Γ of the precipitate in the matrix are particularly hard to obtain, which is why literature values often exhibit a significant spread of values. Γ values for TaC in pure Co range between 0.44 and 2.21 J m⁻².^[38] Also other, more common systems such as aluminum nitride in steel exhibit a wide range, 0.1–2.7 J m⁻².^[39]

The frequency factors and activation energies can be compared with the values of Ta diffusion in Co, which amount to $D = (27 \pm 23) \times 10^{-5} \text{ m}^2 \text{ s}^{-1}$ and $Q = 282.5 \pm 6.0 \text{ kJ mol}^{-1}$, respectively.^[35] This shows that the diffusion of Ta is an important factor for nucleation and growth of the TaC precipitates.

4. Conclusion

The precipitation of nanosized TaC particles in two Co–Re-based alloys was studied with ND and SAS. Volume fraction and size of

the precipitates were obtained and it was shown that addition of Cr yields larger precipitates. These measurements can be carried out in situ and allow a unique view into the processes during cooling of these materials.

A matrix phase transformation is visible, which is correlated with a drop of Ta solubility in the matrix. The corresponding oversaturation results in precipitation. The evolution of the precipitated volume fraction was modeled with a modified KWN approach, which was adapted to cover isochronal cooling processes. Thereby, the activation energies for nucleation and growth of the TaC precipitates could be determined.

The in situ and ex situ scattering data are a sensitive tool to calibrate such models as they are able to measure the precipitation kinetics directly.

5. Experimental Section

Samples: Two Co–Re alloys with TaC precipitates, one without chromium (Co–17Re–0Cr) and one with chromium (Co–17Re–15Cr) added to the alloy matrix, were investigated (see Table 1). The samples were produced by vacuum induction melting from high-purity elemental metals and graphite powder (> 99.8% purity). The bath was superheated to 1900 K under argon atmosphere (175 mbar), where Co melted and readily dissolved Re, Ta, and C into the liquid. The alloys were cast into a metallic mold to obtain 1.2 kg cast blocks. The cast alloys were subjected to a standard three-step homogenizing heat treatment denoted solution treatment (ST): 1623 K for 5 h, 1673 K for 5 h, and 1723 K for 5 h. Argon was quenched to RT. Typically, the polycrystalline material had a grain size of around 100 μm .^[40] The alloy bars were cut after the ST heat treatment into flat 16 \times 16 \times 1 mm³ pieces for in situ SANS measurements or cylinders with 6 mm diameter and 15 mm length for the ND and SAXS measurements. Different samples exhibited slight variations in the transition temperatures but the same qualitative behavior.

Neutron Diffraction: The ND experiments were conducted at the STRESS-SPEC instrument at MLZ^[41,42] while cooling the alloys from 1773 K. Similar measurements were carried out in distinct measurement campaigns on different samples; collated results are shown in this contribution. The samples were stepwise cooled and held at constant temperature for 20 min. The changes between the respective steps were small, $\Delta T = 20 \text{ K}$, to keep the phases near equilibrium. The TaC phase fraction was monitored to determine the temperature-dependent Ta solubility in the Co–Re matrix. The instrument was equipped with a 2D position-sensitive detector that covered an angular range of $\pm 7^\circ$ for one fixed position. The detector was moved to several positions to cover an angular range between 42.5° and 114.5°. As the experiment was conducted slowly enough to keep the phases near equilibrium, the measurements covering different angular ranges were assumed to capture the same state of the sample. A neutron wavelength λ of 1.636(2) Å was used for these experiments. The diffractograms were collected during 10 min of holding for a given detector position. The data evaluation was conducted with the Rietveld method^[43] using the FullProf package^[44]; exemplary Rietveld fits are shown in the Supporting Information.

Small-Angle Scattering: The ex situ SANS measurements were carried out on the SANS-1 instrument at the Heinz-Maier Zentrum (MLZ) in Garching near Munich, Germany.^[45–47] SANS-1 was set up in the three instrument geometries, each with a fixed wavelength: 1) neutron wavelength $\lambda = 6 \text{ Å}$, collimation length: 6 m, and sample-to-detector distance SDD = 2 m; 2) $\lambda = 6 \text{ Å}$, collimation: 8 m, and SDD = 8 m; and 3) $\lambda = 12 \text{ Å}$, collimation: 20 m, and SDD = 20 m. With these settings, a Q -range from 0.01 to 4 nm⁻¹ was covered in a measurement time of 1 h. Data reduction was conducted using the program BerSANS.^[48]

In situ SANS measurements were carried out on D33 at the Institut Laue-Langevin (ILL) in Grenoble, France.^[49] The SANS instrument D33 is a time-of-flight SANS instrument.^[50] A chopper system was used to measure simultaneously with different wavelengths, covering a larger

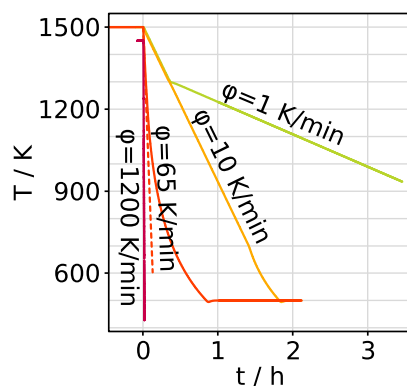


Figure 9. The applied cooling ramps for in situ SAS measurements with their respective nominal cooling rates ϕ . 1, 10, and 65 K min⁻¹ were conducted in neutron experiments using the ILL SANS furnace, whereas the cooling rate 1200 K min⁻¹ was conducted with a dilatometer at the synchrotron. The nominal cooling rate of 65 K min⁻¹ was only reached at the beginning of the cooling process (indicated by the limiting dashed line).

Q -range with a fixed instrument geometry. While the neutron flux at the sample was lower for a single wavelength compared with a monochromatic instrument, comparable count statistics was obtained by adding the scattered signal of various wavelengths for a certain Q -range. A collimation of 7.8 m was used for the incoming cold neutrons and the detector was kept at the fixed SDD 7.8 m. A total wavelength band from 3.0 to 15.0 Å yielded reasonable transmission for the Co–Re alloys. The band was binned into 100 equidistant channels. With this setup, it was possible to get high count statistics within 5 min in the Q -range 0.03 to 3.0 nm⁻¹. The measurement time for each measurement was 10 s. The program Grasp was used for data reduction.^[51]

SAXS experiments with synchrotron X-rays were conducted at the High Energy Material Science Beamline (HEMS) operated by Helmholtz-Zentrum Hereon at Petra III (DESY).^[52] An X-ray wavelength λ of 0.01575 nm was used. A Perkin Elmer XRD1621 image detector with a pixel size of 200 × 200 μm² was used to record the images. With an SDD of 10.8 m, a Q -range from 0.075 to 2.0 nm⁻¹ was accessible. The exact instrument parameters were fitted by analyzing a silver behenate standard.^[53] Images were recorded every 1 s. TA instruments DIL 805A/D quenching dilatometer provided by Helmholtz-Zentrum Hereon was used for the SAXS measurements. The experiments were conducted in argon atmosphere.

The samples were heated with a ramp of 100 K min⁻¹ to $T = 1773$ K and then cooled to RT with different ramps in the in situ experiments, as shown in **Figure 9**. Different continuous cooling ramps of 1, 10, and 65 K min⁻¹ from the supersolus solution temperature at 1773 K were applied in the in situ SANS experiments. In addition, one alloy was rapidly quenched with a ramp of 1200 K min⁻¹ in the in situ SAXS experiment. The temperature histories are shown in **Figure 9**. In case of the slowest cooling ramp, the alloy was cooled faster in the beginning—before any phase transformation was expected—to save measurement time.

All analysis procedures were developed in the software package Matlab v.9.1.

Supporting Information

Supporting Information is available from the Wiley Online Library or from the author.

Acknowledgements

The authors would like to thank Professor Eric J. Mittemeijer for stimulating discussions regarding precipitation kinetics. This work is based

upon experiments conducted at the SANS-1 and STRESS-SPEC instruments operated by GEMS (Hereon) and FRM II (TUM) at the Heinz Maier-Leibnitz Zentrum (MLZ), Garching, Germany. The authors acknowledge DESY (Hamburg, Germany), a member of the Helmholtz Association HGF, for the provision of experimental facilities. Parts of this research were conducted at PETRA III and the authors would like to thank A. Stark for assistance in using the quenching dilatometer provided by Helmholtz-Zentrum Hereon. The authors would also like to thank Institut Laue-Langevin (ILL) in Grenoble, France, for beam time on the instrument D33. P.S. acknowledges support from ESS participation of the Czech Republic, OP (CZ.02.1.01/0.0/0.0/16_013/0001794).

Open access funding enabled and organized by Projekt DEAL.

Conflict of Interest

The authors declare no conflict of interest.

Data Availability Statement

Research data are not shared.

Keywords

in situ measurements, neutron scattering, precipitation kinetics, X-ray scattering

Received: January 31, 2021

Revised: April 20, 2021

Published online:

- [1] J. H. Perepezko, *Science* **2009**, 326, 1068.
- [2] C. T. Sims, *JOM* **1966**, 18, 1119.
- [3] J. Sato, *Science* **2006**, 312, 90.
- [4] J. Rösler, D. Mukherji, T. Baranski, *Adv. Eng. Mater.* **2007**, 9, 876.
- [5] L. Karge, Dissertation, Technische Universität München, München **2018**.
- [6] R. Gilles, D. Mukherji, L. Karge, P. Strunz, P. Beran, B. Barbier, A. Kriele, M. Hofmann, H. Eckerlebe, J. Rösler, *J. Appl. Crystall.* **2016**, 49, 1253.
- [7] L. Karge, R. Gilles, D. Mukherji, P. Strunz, P. Beran, M. Hofmann, J. Gavilano, U. Keiderling, O. Dolotko, A. Kriele, A. Neubert, J. Rösler, W. Petry, *Acta Mater.* **2017**, 132, 354.
- [8] T. Depka, F. Benesch, C. Somsen, D. Mukherji, V. Yardley, G. Eggeler, J. Rösler, in *Proc. of the 12th Int. Conf. on Creep and Fracture of Engineering Materials and Structures*, Japan Institute of Metals, Sendai **2012**, pp. 1–4.
- [9] M. Heilmaier, J. Rösler, D. Mukherji, M. Krüger, *Development of Novel Metallic High Temperature Materials by Microstructural Design*, John Wiley & Sons, Ltd **2013**, pp. 467–493, chapter 19.
- [10] L. Karge, R. Gilles, D. Mukherji, A. Stark, P. Beran, N. Schell, M. Hofmann, P. Strunz, J. Häusler, J. Rösler, *Mater. Sci. Eng.: A* **2018**, 719, 124.
- [11] P. Strunz, D. Mukherji, P. Beran, R. Gilles, L. Karge, M. Hofmann, M. Hoelzel, J. Rösler, G. Farkas, *Met. Mater. Int.* **2018**, 24, 934.
- [12] P. Strunz, D. Mukherji, P. Beran, R. Gilles, M. Hofmann, L. Karge, J. Rösler, G. Farkas, *Acta Phys. Polon. A* **2018**, 134, 829.
- [13] P. Beran, D. Mukherji, P. Strunz, R. Gilles, L. Karge, M. Hofmann, M. Hoelzel, J. Rösler, G. Farkas, *Metals* **2018**, 8, 621.

- [14] D. Mukherji, J. Rösler, M. Krüger, M. Heilmaier, M.-C. Bölitz, R. Völkl, U. Glatzel, L. Szentmiklósi, *Scr. Mater.* **2012**, 66, 60.
- [15] L. Karge, R. Gilles, D. Mukherji, P. Beran, P. Strunz, M. Hölzel, J. Rösler, *Phys. B* **2017**, 132, 354.
- [16] L. Wang, B. Gorr, H.-J. Christ, D. Mukherji, J. Rösler, *Oxid. Met.* **2013**, 80, 49.
- [17] L. Wang, B. Gorr, H.-J. Christ, D. Mukherji, J. Rösler, *Oxid. Met.* **2015**, 83, 465.
- [18] P. Beran, D. Mukherji, P. Strunz, R. Gilles, M. Hölzel, J. Rösler, *Adv. Mater. Sci. Eng.* **2018**, 2018, 5410871.
- [19] K. Esleben, B. Gorr, H.-J. Christ, C. Pritzel, D. Mukherji, J. Rösler, P. Beran, P. Strunz, M. Hoelzel, R. Gilles, *Int. J. Mater. Res.* **2019**, 110, 1092.
- [20] R. Gilles, *J. Surf. Invest.* **2020**, 14, S69.
- [21] R. Gilles, D. Mukherji, H. Eckerlebe, L. Karge, P. Staron, P. Strunz, T. Lippmann, *J. Alloys Compd.* **2014**, 612, 90.
- [22] D. Mukherji, P. Strunz, S. Piegert, R. Gilles, M. Hofmann, M. Hölzel, J. Rösler, *Metall. Mater. Trans. A* **2012**, 43, 1834.
- [23] B. Strauss, F. Frey, W. Petry, J. Trampenau, K. Nicolaus, S. M. Shapiro, J. Bossy, *Phys. Rev. B* **1996**, 54, 6035.
- [24] J. Coakley, V. A. Vorontsov, K. C. Littrell, R. K. Heenan, M. Ohnuma, N. G. Jones, D. Dye, *J. Alloys Compd.* **2015**, 623, 146.
- [25] R. N. Andrews, J. Serio, G. Muralidharan, J. Ilavsky, *J. Appl. Crystall.* **2017**, 50, 734.
- [26] Neutron Activation and Scattering Calculator, <https://www.ncnr.nist.gov/resources/activation/> (accessed: January 2021).
- [27] A. A. Rempel', *Phys.-Uspekhi* **1996**, 39, 31.
- [28] A. Guinier, G. Fournet, *Small-Angle Scattering of X-Rays*, Structure of Matter Series, Wiley, New York/Chichester, UK **1955**.
- [29] P. Beran, D. Mukherji, P. Strunz, R. Gilles, M. Hofmann, L. Karge, O. Dolotko, J. Rösler, *Met. Mater. Int.* **2016**, 22, 562.
- [30] I. Breßler, J. Kohlbrecher, A. F. Thünemann, *J. Appl. Crystall.* **2015**, 48, 1587.
- [31] R. Kampmann, R. Wagner, in *Proc. 2nd Acta-Scripta Metall. Conf.*, Pergamon, Oxford. **1984**, pp. 91–103.
- [32] M. Perez, M. Dumont, D. Acevedo-Reyes, *Acta Mater.* **2008**, 56, 2119.
- [33] F. Liu, F. Sommer, E. Mittemeijer, *J. Mater. Sci.* **2004**, 39, 1621.
- [34] R. Bauer, B. Rheingans, E. Mittemeijer, *Metall. Mater. Trans. A* **2011**, 42, 1750.
- [35] S. Neumeier, H. Rehman, J. Neuner, C. Zenk, S. Michel, S. Schuwalow, J. Rogal, R. Drautz, M. Göken, *Acta Mater.* **2016**, 106, 304.
- [36] Y. Iijima, F. Makuta, R. P. Agarwala, K. Hirano, *Mater. Trans. JIM* **1989**, 30, 984.
- [37] V. A. Baheti, S. Santra, S. Roy, K. Perumalsamy, S. Prasad, R. Ravi, A. Paul, *J. Alloys Compd.* **2015**, 622, 1033.
- [38] V. Sarin, *Comprehensive Hard Materials*, Elsevier, Amsterdam/New York **2014**.
- [39] A. Costa e Silva, *TMS 2015 144th Annual Meeting & Exhibition*, Springer International Publishing, Cham **2016**, pp. 1409–1416.
- [40] A. K. Czerny, D. Mukherji, J. Rösler, *Pract. Metall.* **2014**, 51, 499.
- [41] M. Hofmann, R. Schneider, G. Seidl, J. Rebelo-Kornmeier, R. Wimpory, U. Garbe, H.-G. Brokmeier, *Phys. B* **2006**, 385–386, 1035.
- [42] Heinz Maier-Leibnitz Zentrum, *J. Large-Scale Res. Facil.* **2015**, 1, A6.
- [43] H. M. Rietveld, *J. Appl. Crystall.* **1969**, 2, 65.
- [44] J. Rodríguez-Carvajal, *Phys. B* **1993**, 192, 55.
- [45] R. Gilles, A. Ostermann, C. Schanzer, B. Krimmer, W. Petry, *Phys. B* **2006**, 385, 1174.
- [46] S. Mühlbauer, A. Heinemann, A. Wilhelm, L. Karge, A. Ostermann, I. Defendi, A. Schreyer, W. Petry, R. Gilles, *Nucl. Instrum. Methods Phys. Res. Sect. A* **2016**, 832, 297.
- [47] Heinz Maier-Leibnitz Zentrum, *J. Large-Scale Res. Facil.* **2015**, 1, A10.
- [48] U. Keiderling, *Appl. Phys. A: Mater. Sci. Process.* **2002**, 74, 1455.
- [49] L. Karge, R. Gilles, D. Honecker, D. Mukherji, P. Strunz, In-Situ SANS Study on Influence of Boron Addition on TaC Precipitate Stability in Co-Re Alloys at High Temperatures, Institut Laue-Langevin (ILL) **2016**, <https://doi.org/10.5291/ILL-DATA.1-01-150>.
- [50] C. D. Dewhurst, I. Grillo, D. Honecker, M. Bonnaud, M. Jacques, C. Amrouni, A. Perillo-Marcone, G. Manzin, R. Cubitt, *J. Appl. Crystall.* **2016**, 49, 1.
- [51] C. Dewhurst, *Grasp* **2008**, <https://www.ill.eu/users/scientificgroups/large-scale-structures/grasp/>.
- [52] N. Schell, A. King, F. Beckmann, T. Fischer, M. Müller, A. Schreyer, *Mechanical Stress Evaluation by Neutrons and Synchrotron Radiation VI, Volume 772 of Materials Science Forum*, Trans Tech Publications Ltd **2014**, pp. 57–61.
- [53] R. Gilles, U. Keiderling, P. Strunz, A. Wiedenmann, H. Fuess, *Mater. Sci. Forum* **2000**, 321–324, 264.
- [54] N. Wanderka, M. S. Mousa, P. Henke, O. Korchuganova, D. Mukherji, J. Rösler, J. Banhart, *J. Mater. Sci.* **2016**, 51, 7145.